Computers and Chemical Engineering 148 (2021) 107267

Contents lists available at ScienceDirect

Computers and Chemical Engineering

journal homepage: www.elsevier.com/locate/compchemeng

Integration of feedback control and run-to-run control for plasma enhanced atomic layer deposition of hafnium oxide thin films

Sungil Yun[a], Yangyao Ding[a], Yichi Zhang[a], Panagiotis D. Christofides[a,b,*]

[a] Department of Chemical and Biomolecular Engineering, University of California, Los Angeles, CA, 90095-1592, USA
[b] Department of Electrical and Computer Engineering, University of California, Los Angeles, CA 90095-1592, USA

ARTICLE INFO

Article history:
Received 5 February 2021
Revised 22 February 2021
Accepted 23 February 2021
Available online 1 March 2021

Keywords:
Plasma-enhanced atomic layer deposition
Computational fluid dynamics
Kinetic Monte-Carlo model
PI control
Run-to-run control

ABSTRACT

Facilitated by the increasing importance and demand of semiconductors for the smartphone and even the automobile industry, the plasma-enhanced atomic layer deposition (PEALD) has gained tremendous industrial interest as it offers a way to efficiently deposit thin-films with ultra-high conformity. A series of studies have been carried out to elucidate the mechanisms and the concept of the PEALD process. Despite the great deal of research effort, PEALD processes have not been fully characterized from the view point of process control. This study aims to use a previously developed multiscale computational fluid dynamics (CFD) simulation model to design and evaluate an optimized control scheme to deal with industrially-relevant disturbances. Specifically, an integrated control scheme using a proportional-integral (PI) controller and a run-to-run (R2R) controller is proposed and evaluated to ensure the deposition of high-quality conformal thin-films. The PEALD process under typical disturbances is simulated using the multiscale CFD model, and the integrated controller is applied in the process domain. Using the controller parameters determined from the open-loop results, the developed integrated PI-R2R controller successfully mitigates the disturbances in the operating pressure and the gas bubbler temperature with the combined effort of both controllers.

1. Introduction

The continuous advancement and achievement of breakthroughs in semiconductor technologies and the increasing growth of the semiconductor market have been leading to the enormous investment for the development of thin-film materials. Thin film materials, as a crucial and fundamental component of the entire semiconductor industry, have been extensively investigated with the high priority to enable the microelectronic devices to be miniaturized further. The shrinking of the devices greatly reduces the overall dimension of the end product including personal computers and smart phones. To implement miniaturization, high-κ thin-film materials have received attention, which have better thermal stability and excellent performance in capacitance and charge mobility compared to the traditional gate oxide SiO_2. Despite the apparent advantages of high-κ materials such as TiO_2 (Kukli et al., 2000), HfO_2 (Liu et al., 2005), Al_2O_3 (Gakis et al., 2019a; 2019b) and ZrO_2 (Yun et al., 2004), it is challenging to deposit high-κ materials through the ALD process due to the associated issues including the halogen atom residue in films, high impurity contamination, and slow deposition rate.

To tackle these issues, PEALD has been proposed as a substitute of the ALD due to a variety of significant benefits. First of all, the PEALD features the utilization of high-energy species (Won et al., 2005), which allows the reduction of the temperature requirement and the increase in the reactivity of the precursors. Therefore, PEALD is particularly effective for the temperature-sensitive materials (Joo and Rossnagel, 2009). In addition, the PEALD is expected to reduce the contamination and the energy consumption, and enhance the deposition throughput. As one of the most important thin-film materials, the deposition HfO_2 using PEALD has not been yet extensively characterized. Thus, this work focuses on the PEALD process for the deposition of HfO_2 thin-films as a promising high-κ material.

In PEALD, two crucial operating factors are considered. First, the selection of precursors should be carefully performed. Specifically, for the deposition of HfO_2 thin-film via PEALD, amino-containing metal organic compounds, such as tetrakis(dimethylamino)hafnium (TDMAHf), tetrakis(ethylmethylamino)hafnium (TEMAHf), and

* Corresponding author at: Department of Chemical and Biomolecular Engineering, University of California, Los Angeles, CA, 90095-1592, USA.
E-mail address: pdc@seas.ucla.edu (P.D. Christofides).

https://doi.org/10.1016/j.compchemeng.2021.107267
0098-1354/

tetrakis(diethylamino)hafnium (TDEAHf), are often used as the hafnium precursors due to the spontaneous formation of N-H hydrogen bonds that reduces the energy barrier (Kukli et al., 2000; Liu et al., 2003; Shi et al., 2011). On the other hand, for the oxygen precursor of the high energy plasma, a variety of choices have been studied, including ozone plasma, water plasma and oxygen plasma (Rai et al., 2010; Kanomata et al., 2014). Second, the reactor design and configuration also greatly impact the produced thin-film material. Although the deposition occurs on the wafer surface, the quality of the final product is highly dependent on the gas-phase transport profile development in the main reactor chamber. Despite the variety of existing plasma reactor designs, remote plasma reactor, which is the focus of this work, is considered as the most balanced and suitable option to implement the PEALD process. A distant plasma source is used in remote plasma reactors to protect the substrate surface from the potential damage caused by sputtering, i.e., the bombardment of the film by excessive high-energy radicals (Won et al., 2014; Jeon et al., 2007).

Although the PEALD has many benefits, it has also restrictions such as high operation cost and operational complexity. One approach to address its limitations (Lee et al., 2006; Profijt et al., 2011) is multiscale modeling, which provides a holistic perspective of the PEALD process. Therefore, the simulation results are extremely helpful to understand the complicated interaction between the microscopic surface domain and the macroscopic gas-phase domain. Moreover, many studies have focused on the characterization of the thermal ALD and the PEALD using simulation. For example, an inductively coupled plasma (ICP) reactor was characterized by a simulation model created by Tinck and Bogaerts (2011). Gerogiorgis and Ydstie (2005), and Epelle and Gerogiorgis (2017) also attempted to model the gas transport domain using the CFD model. While most of the studies focus on either the gas-phase or the microscopic domain, originally inspired by Crose et al. (2015), Zhang et al. (2020b) has proposed an efficient way to connect both domains in an integrated multiscale CFD model. Based on previous efforts by Ding et al. (2019), Ding et al. (2020), and Zhang et al. (2019), the constructed multiscale CFD model has been able to accurately characterize the entire process domain of PEALD, and the methodology and results have been validated by experimental data. Moreover, by applying machine-learning techniques, Ding et al. (2021) derived a data-driven model tailored for the PEALD process, from which a set of optimal operating condition was derived.

All aforementioned series of work on the detailed and efficient models has cleared the obstacles to construct a reliable control scheme for the PEALD operation. Due to the sensitivity of the deposition quality to various operating parameters, the process disturbance should be carefully and efficiently mitigated. Although Zhang et al. (2020a) developed an integrated feedback control scheme for the batch thermal ALD system, currently there still lacks a proper guideline to perform process control for the PEALD system. Thus, in this study, inspired by Zhang et al. (2020a), a novel control methodology that integrates proportional-integral (PI) control and run-to-run (R2R) control is used to eliminate the effect of disturbances in the operating pressure and the precursor bubbler temperature. The contribution from both controllers complements one another, and the result is demonstrated through the dedicated case study of the developed multiscale CFD model.

2. Multiscale CFD modeling of PEALD

The following section covers a brief introduction for the previously developed HfO_2 PEALD multiscale CFD model, while more specific details and specifications can be found in Zhang et al. (2020b). In total, three domains are discussed. The macroscopic scale involves two domains characterized by the CFD: the ICP plasma generation domain and the gas-phase transfer domain. The microscopic scale is characterized by the surface deposition reaction domain, which is described by the kinetic Monte-Carlo (kMC) method (Fig. 1).

2.1. Macroscopic modeling

As mentioned in Section 1, the inductively coupled plasma (ICP) reactor is characterized based upon the Gaseous Electronics Conference (GEC) cell proposed by the National Institute of Standards and Technology (NIST). The modeled plasma reactor uses magnetically activated species as a high quality plasma source. The plasma chamber configuration is shown in Fig. 2.

The ICP plasma generator uses the alternating current (AC) to induce the magnetic field, in which the operating power of the AC generator is set to 2000 W, and the radio-frequency (RF) of the current is 13.56 MHz. The Ampere-Maxwell equation is used for modeling the electromagnetic field:

$$\vec{\nabla}\left(\epsilon_f \vec{B}\right) = \vec{J} + \epsilon_o \frac{\partial \vec{E}}{\partial t} \tag{1}$$

where ϵ_f is the electric permeability of materials, $\vec{B}$ is the magnetic field, $\vec{J}$ is the current density, ϵ_o is the electric permeability of free space, $\vec{E}$ is the electric field, and t is the time.

The two neutral species, oxygen and argon, are fed into the ICP plasma chamber throughout the entire deposition process. Argon is used as a carrier gas and it is constantly injected into the ICP chamber to maintain a baseline pressure. When the oxygen plasma precursor is required, the oxygen injection valve is activated and oxygen is pumped into the ICP chamber and, at the same time, the magnetic field is activated to generate the plasma species. The details on the plasma generation reactions involving both argon and oxygen can be found in Zhang et al. (2020b), as well as their corresponding kinetic parameters. In this work, COMSOL Multiphysics is used to solve the plasma domain profile through finite element method. Based on the given operating conditions and boundary conditions, a frequency-transient solution for the plasma profile is solved. The typical time-scale for the achievement of steady-state inside the ICP plasma generator is around 10^{-3} s, which is significantly faster than that of the main reactor chamber. Therefore, the plasma generation domain can be decoupled from the reactor chamber domain without sacrificing the accuracy of the solution in that the interaction between the two domains are minimal. Specifically, the computed plasma profile towards the ICP chamber outlet is used as the inlet profile of the main reactor chamber.

The quality of the deposited HfO_2 thin-film is strongly related to the microscopic surface reactions, of which the dynamics is directly influenced by the macroscopic gas profile of the main reactor chamber. In this paper, the ASM International EmerALD XP reactor, as a prototype, was used and the geometry optimization was performed to achieve the optimal concentration uniformity on the surface (Lee et al., 2006; Zhang et al., 2020b). As shown in Fig. 3, the horn-shaped reactor is adopted that provides the essential guidance of the inlet gas flow and the uniformly developed flow distribution. In the reactor chamber, the gas species travel to the substrate surface and react with the surface species. Unused precursors and carrier gas are then purged from the reactor with a vacuum pump. Although the dynamic pressure inside the reactor may vary due to the precursor injection and gas purging, the vacuum pump maintains the operating pressure of 100 Pa under the constant flow of 300 sccm Ar at the inlet. In addition, the bubbler to generate the inlet stream is not explicitly constructed, which operates at the temperature of 348.15 K to achieve the precursor vapor pressure of 133 Pa (Hausmann et al., 2002). Ansys Fluent uses

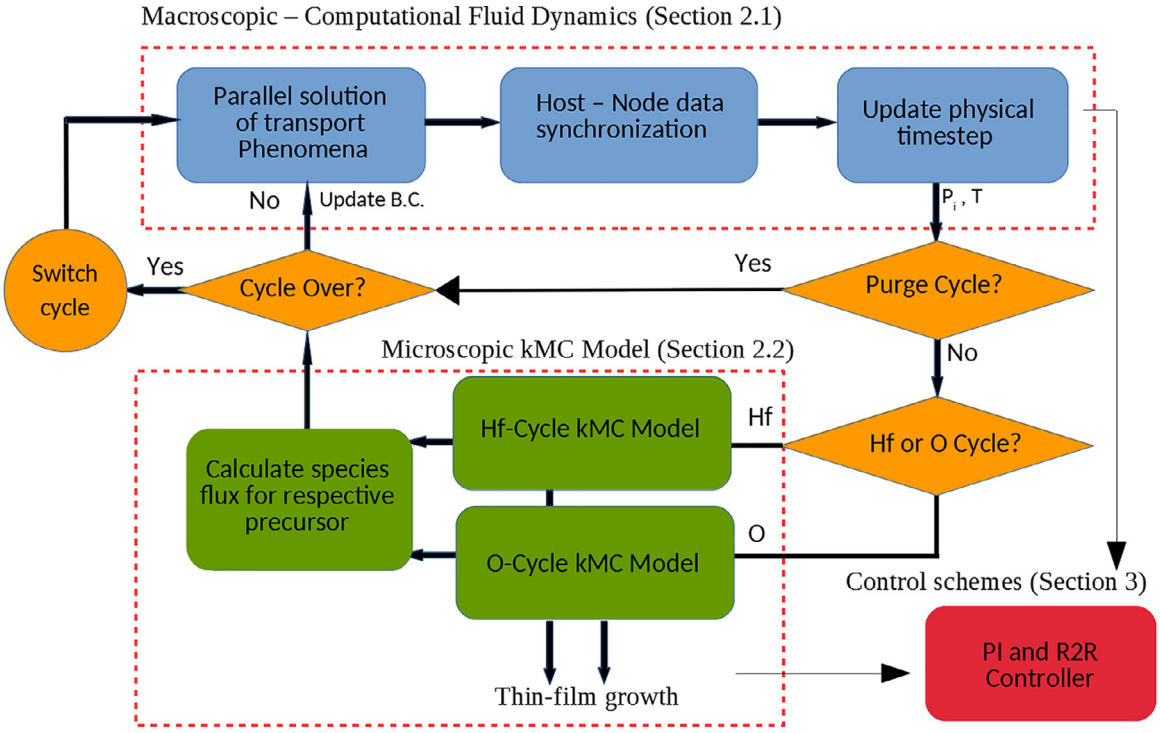

Fig. 1. An overview of the multiscale CFD model and workflow.

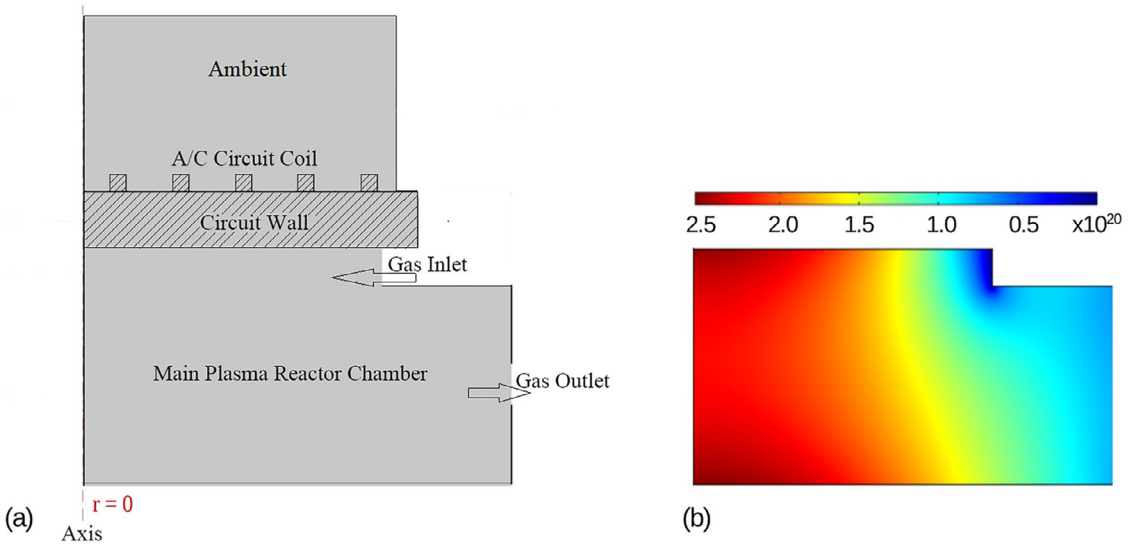

Fig. 2. (a) The cross-sectional view of the plasma reactor. Shaded area represents solid regions of circuit wall and circuit coils. Unshaded area represents fluid regions. The arrows represent the directions of the flow at inlet and outlet. (b) The number density distribution of O radical in the plasma reactor.

finite volume method to solve the governing equations of momentum, energy, and species transfer, which are shown as below in the tensor form (Fluent, 2013):

$$\frac{\partial}{\partial t}(\rho E) + \nabla(\vec{v}(\rho E + P)) = \nabla(k\nabla T - \Sigma h\vec{J} + (\bar{\bar{\tau}}\vec{v})) + S_h \tag{2}$$

$$\frac{\partial(\rho\vec{v})}{\partial t} + \nabla\cdot(\rho\vec{v}\vec{v}) = -\nabla P + \nabla\cdot(\bar{\bar{\tau}}) + \rho\vec{g} + \vec{F} \tag{3}$$

$$\bar{\bar{\tau}} = \mu\left[\left(\nabla\vec{v} + \nabla\vec{v}^{T}\right) - \frac{2}{3}\nabla\cdot\vec{v}I\right] \tag{4}$$

$$\frac{\partial}{\partial t}(\rho Y_i) + \nabla\cdot(\rho\vec{v}Y_i) = -\nabla\cdot\vec{J_i} + R_i + S_i \tag{5}$$

$$\vec{J_i} = -\rho D_{m,i}\nabla Y_i - D_{T,i}\frac{\nabla T}{T} \tag{6}$$

$$\vec{R_i} = M_{w,i}\sum_{r=1}^{N_r} R_{i,r} \tag{7}$$

where ρ is the fluid density, E is the internal energy of the fluid, $\vec{v}$ is flow field velocity, P is the static pressure of the system, T is the flow field temperature, k is the thermal conductivity, $\bar{\bar{\tau}}$ is the stress tensor, h is the enthalpy, $\vec{J}$ is the fluid diffusion flux, $\vec{g}$ is the gravity, F is the external force exerted on the flow field, μ is the viscosity, I is the unit tensor, Y is the mass fraction, S_h, R

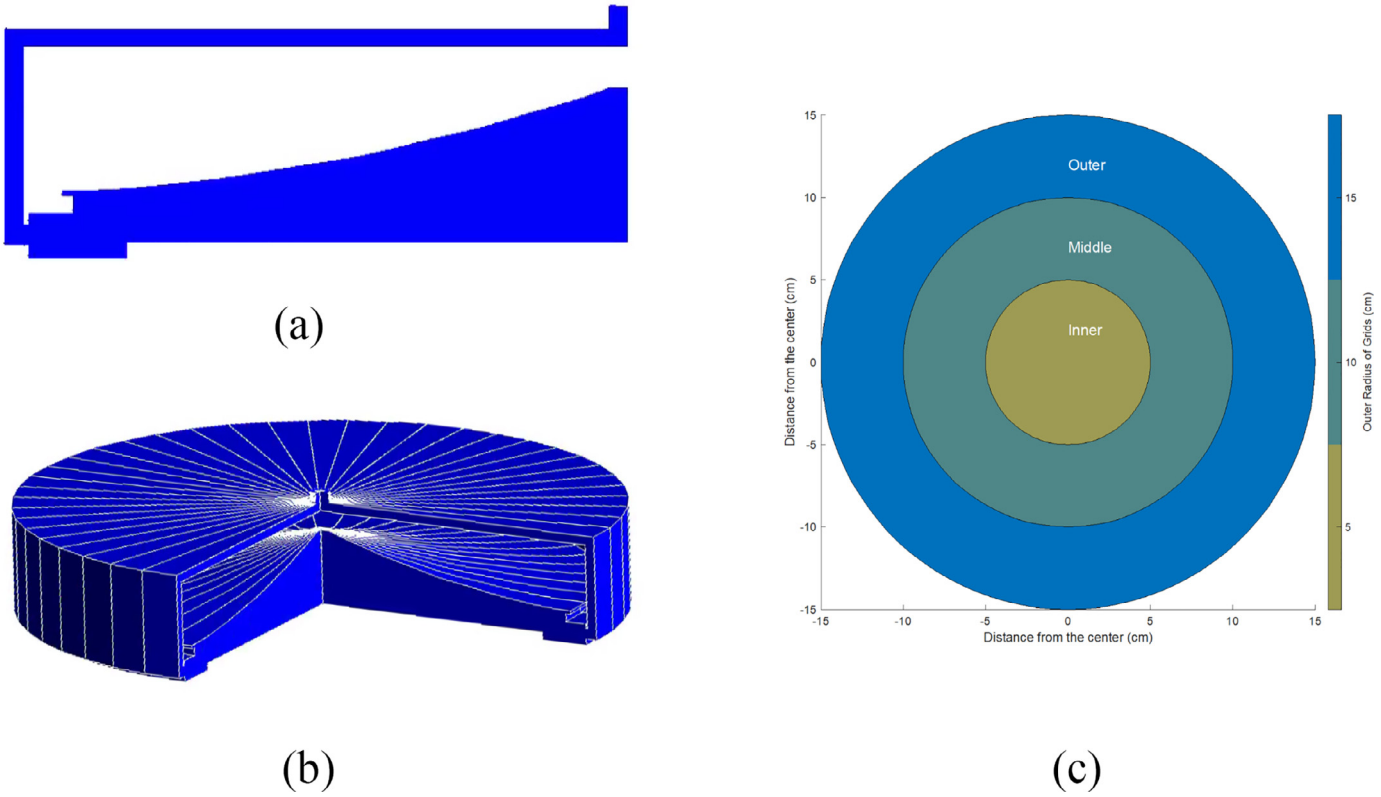

Fig. 3. (a) Reactor geometry used in the 2D axisymmetric model. (b) Reactor geometry used in the full 3D model. (c) Demonstration of the three wafer regions (inner, middle, and outer) versus the distance from the wafer center.

and S are the heat, reactions and mass transfer source terms, respectively, and D_m and D_T are the mass and thermal diffusivities. $\vec{R}$ is the total reaction rate, M_w denotes the molecular mass, N_R is the total number of reactions, and R_r is the individual rate of generation/consumption, which is governed by the rate constant. For all the above variables, subscript i refers to the ith species. More details regarding the specifications of the reactor geometry, CFD theory and model setting can be found in Zhang et al. (2020b).

2.2. Microscopic surface model

A microscopic surface model for the deposition of HfO_2 thin-film was described in Ding et al. (2020). Here, a brief introduction of the developed microscopic model is presented, including the structural assumption of the HfO_2 thin-film, deposition reaction sets and corresponding kinetic rates, and the formulation of the 3D kMC model. At low temperature, which is the characteristic of the PEALD process, HfO_2 typically appears in monoclinic structure Kumar et al. (2017). For the initial stage of the PEALD cycles, the hydroxylated monoclinic (111) surface is used as the favored starting surface as shown in Fig. 4. Although it is desirable to capture the entirely realistic lattice domain, an approximated tetrahedral lattice is adopted to reduce the computation demand, similar to the methodology used by Ding et al. (2019) to capture the deposition of SiO_2 using thermal ALD. This approximation, however, maintains the connectivity between elements and the layer periodicity observed in the real lattice. In addition, the size of the simulated lattice is set to be $1200\times1200\times N_{layer}$ to ensure size-independence of the simulation result, where N_{layer} is the total number of layers deposited (Huang et al., 2010).

The PEALD process shares the similar alternating half-cycle scheme with the traditional thermal ALD. During each half-cycle, each precursor stream will be introduced into the reactor and surface reactions occur, where the atoms of the desired element are chemically deposited to the current surface. A common choice for the Hf-Cycle precursor is TDMAHf. During the Hf-Cycle reactions, TDMAHf undergoes a series of dissociative chemisorption steps, where the dimethylamine (DMA) groups from the TDMAHf molecule are released, so that a bond can be formed between the Hf atom and the surface oxygen atom. For the O-Cycle, oxygen plasma is used as the precursor, which contains molecular oxygen, atomic oxygen, as well as the derived high energy oxygen radicals and ions. Plasma reactions are usually highly complex. However, from existing literature, we were able to establish a simplified, yet chemically comprehensive, reaction set to reduce the computational complexity (Jeon and Won, 2008; Shirazi and Elliott, 2014). The reaction mechanism used in this work is shown in Fig. 5. Essentially, during the introduction of oxygen plasma, the surface DMA groups from the previous Hf cycle are oxidized and replaced with hydroxyl groups, which enable the further deposition of the next half-cycle.

In the developed microscopic model, reaction rates are computed using the transition state theory (TST) and the collision theory (Cortright and Dumesic, 2001). From the TST theory, the rates of thermodynamically activated reactions follow the general Arrhenius-type rate equation as follows,

$$r_{rxn} = A\exp\left(\frac{-E_a}{RT}\right) \tag{8}$$

where E_a is the activation energy of the transition state complex, A is the pre-exponential factor of the Arrhenius equation, R is the universal gas constant, and T is the surface temperature of the substrate. On the other hand, for the athermal gas-surface reactions, of which the activation energy is not well-defined, the collision theory is used to describe the kinetic rates of those reactions. The reaction rate formulation using the collision theory is demonstrated

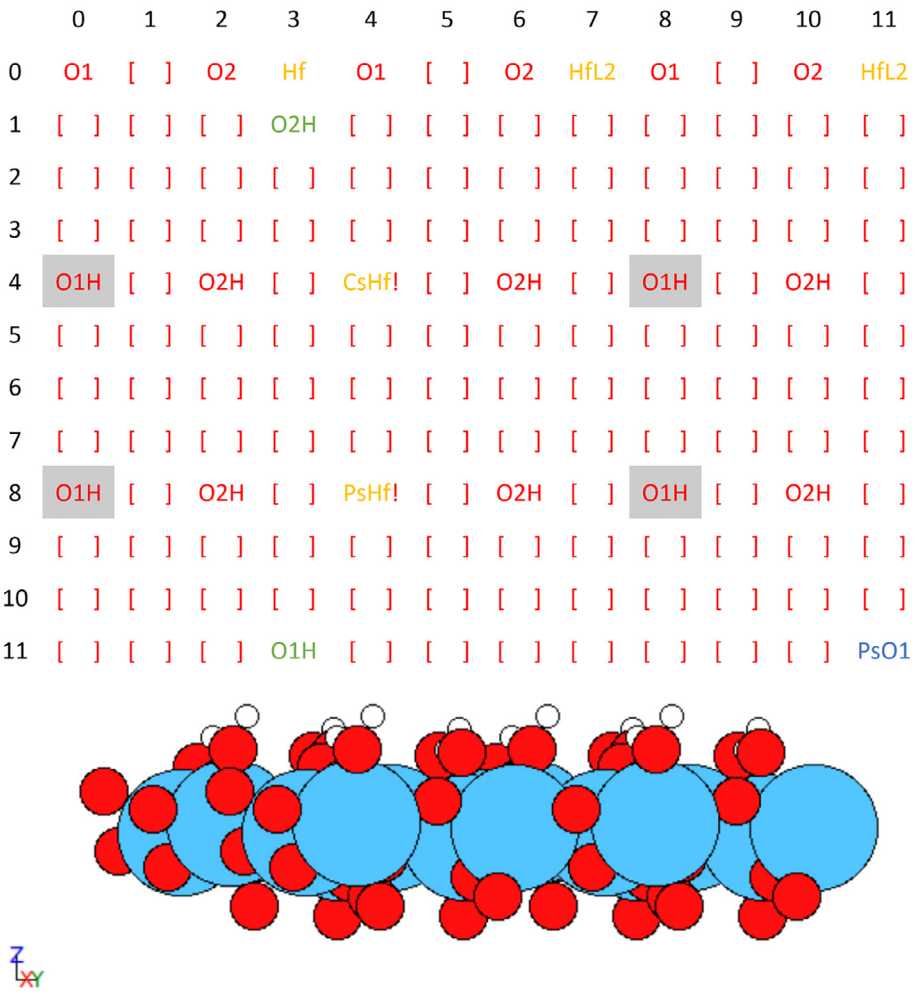

Fig. 4. The representation of the simplified lattice and the fully-hydroxylated surface slab of HfO_2. Top: The approximated lattice with examples of adsorbed species. PsHf and CsHf represent the physisorbed and chemisorbed precursor, respectively, HfL2 represents the deposited Hf terminated with two dimethylamino ligands, and PsO1 and PsO2 represent two distinctively physisorbed oxygens, respectively. Bottom: hydroxyl-terminated HfO_2 slab.

as follows,

$$r_{phs} = \frac{p}{RT}\sqrt{\frac{8RT}{\pi m}} s_c N_a \sigma \tag{9}$$

where m is the precursor molar mass, σ is the surface area of the lattice unit cell, N_a is the Avogadro number, and s_c is the sticking coefficient, of which the values are obtained from Dorsmann and Kleijn (2007).

As mentioned in Section 1, the microscopic surface dynamics is modeled using the kinetic Monte-Carlo (kMC) method. Specifically, a customized n-fold hybrid kMC algorithm developed in Ding et al. (2019) is used. Following the kMC procedure, reactions are selected and the corresponding time progression is determined. In the kMC algorithm, an important parameter is the total reaction rate, r_{total}, which is calculated as the sum of all reaction rates,

$$r_{total} = \sum_{i=1}^{N} r_i \tag{10}$$

where r_i represents the individual reaction rate of a system of N individual reactions, which are arranged in an arbitrary order. After the total reaction rate is found, a random number, $\gamma_1 \in (0, 1]$, is generated to determine the reaction that will occur next using its associated normalized indicator, $l_i \in (0, 1]$, which is the total normalized probabilities of the previous events in terms of the arbitrary order:

$$l_i = \frac{\sum_{j=1}^{i} r^j_{unweighted} C_j}{\sum_{k=1}^{N} r^k_{unweighted} C_k}, \quad i = 1, ..., N \tag{11}$$

where the unweighted rate of reaction, $r_{unweighted}$, will be weighted according to the concentration of the reactant, C. For example, if the generated random number falls between l_{i-1} and l_i, then the ith reaction will be carried out next. The detail of the rate computation can be found in Ding et al. (2020). Additionally, for the time progression of the system, a second random number $\gamma_2 \in (0, 1]$ is generated and the time of each reaction, regardless of its individual rate, is computed as follows:

$$\Delta t = \frac{-\ln \gamma_2}{r_{total}} \tag{12}$$

3. Control scheme

The stringent quality requirement of PEALD demands the operating conditions to be consistent throughout the entire deposition process. Therefore, disturbances to the reactor operations must be effectively evaluated in various deposition processes to ensure the final film quality. Traditionally, feedback control systems have been used to eliminate the effect of disturbances in

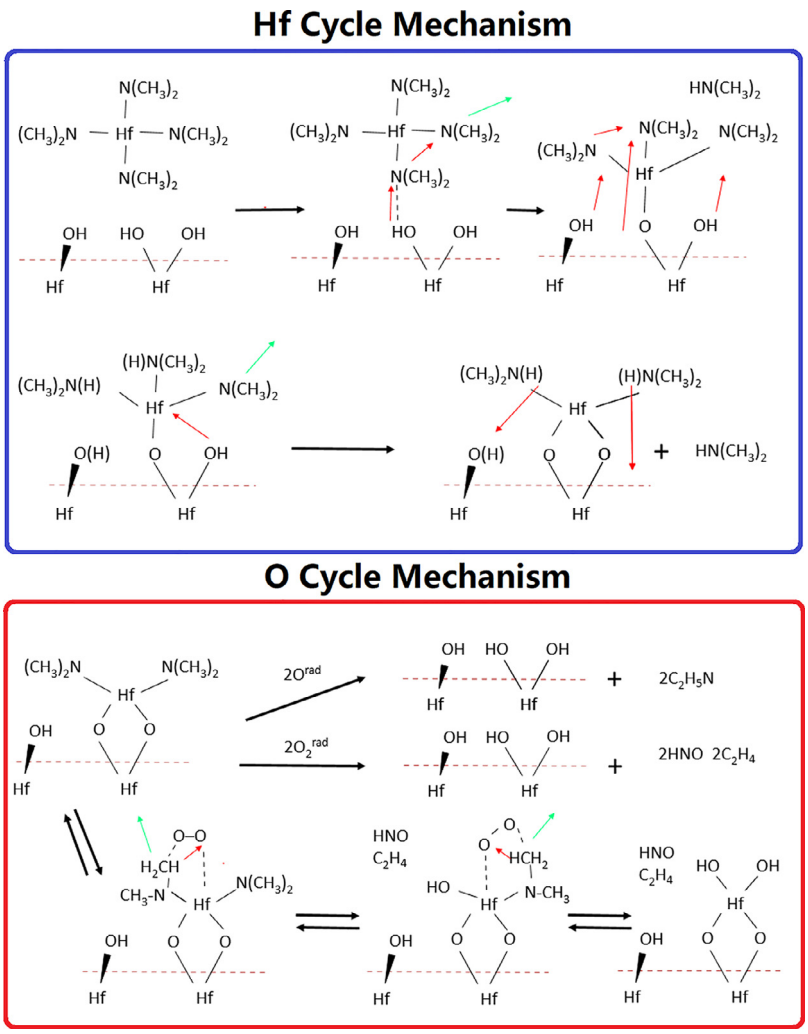

Fig. 5. The adopted reaction mechanisms for both half cycles. The black arrows represent the reaction set, and the red arrows represent the diffusion of protons. (For interpretation of the references to color in this figure legend, the reader is referred to the web version of this article.)

real-time. The performance of the feedback control has been extensively proved in various processes, including the application of plasma enhanced chemical vapor deposition (PECVD) (Armaou and Christofides, 1999), which is very similar to PEALD. In the feedback control system the measurement of the control variable is constantly fed back to the controller. The controller then compares the deviation of the measured value with the set point value and sets it as the process error. To offset the error, the controller changes the manipulated variable through an actuator, such as pressure regulating valves or flow control valves.

Three types of feedback controllers are commonly used for the real-time closed-loop system: the proportional (P) controller, the proportional-integral (PI) controller, and the proportional-integral-derivative (PID) controller. The integral (I) mode is essential to ultimately eliminate the residual error. In the present work, PI control is used instead of PID control, as PI control allows for a desired closed-loop response without offset while PID control may lead to sensitivity to sensor noise due to the derivative term. Specifically, the PI controller adjusts the inlet mass flow rate to maintain the desired partial pressure of the TDMAHf precursor. A typical pressure sensor that can be used for the feedback control system considered in this work is AST20HA pressure transducer manufactured by American Sensor Technologies, Inc., and a common choice for the flow rate actuator is the SmartTrak50 mass flow controller from Sierra Instruments. Additionally, the real-time measurement of the molar fraction can be achieved by using the HPR-20 real-time GC gas analysis system manufactured by Hiden Analytics, of which the result can be used to compute the partial pressure of the precursor.

Nevertheless, due to the limitation on control actions and the relatively short process time-scale of the PEALD, a feedback controller alone, even an advanced controller like a model predictive controller (MPC), may not be able to fully counter the effect of disturbances. As a result, similar to Crose et al. (2019), a run-to-run (R2R) controller is used along side the PI controller to adjust process parameters across multiple batches that can not be adjusted in real-time. Specifically, the R2R controller adjusts the TDMAHf molar fraction of the inlet stream to ensure the full coverage through the mixing ratio of carrier gas and precursor flow rate. The adjustment is performed based on a empirically determined input-output relationship between the inlet TDMAHf molar fraction and the final film coverage, and the control action can be also actuated through the aforementioned mass flow controller. Using the developed multiscale CFD model, the parameters of the PI controller and the R2R controller are identified and tuned, and both controllers are integrated to ensure the full coverage on the wafer under disturbances.

The feedback controller-only results and the integrated feedback-R2R controller results are presented in the following sections.

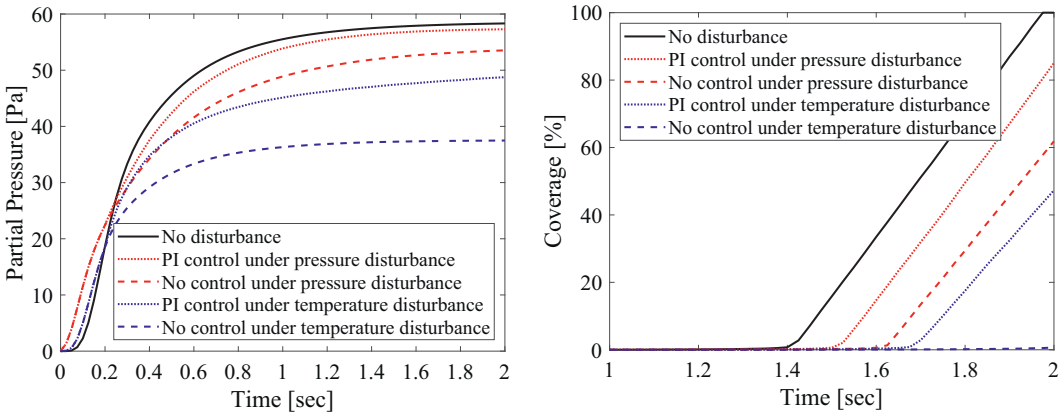

Fig. 6. The development of process variables over process time for various operating conditions and controller actions. The black solid line represents the result without disturbance. The red dotted line represents the result with disturbance and with control action from the PI controller. The red dashed line represents the result with disturbance in pressure but without control action from the PI controller. The blue dotted line represents the result with disturbance and with control action from the PI controller. The blue dashed line represents the result with disturbance in temperature but without control action from the PI controller. (a) Precursor partial pressure over process time. (b) Film coverage over process time. (For interpretation of the references to color in this figure legend, the reader is referred to the web version of this article.)

3.1. Disturbances and open-loop simulation results

The first disturbance considered in this work is the variation in the operating pressure. The PEALD process is typically operated near vacuum and the surface reaction rate is very sensitive to pressure change. Therefore, even a small deviation in the operating pressure can cause a significant effect on the wafer coverage. Such deviation can be induced by the malfunctioning of the vacuum pump. In the scenario where the vacuum pump experiences a power surge, a sudden increment in pump power could result in the reduction of the operating pressure. In this work, a case study is performed when the operating pressure of 100 Pa, which is the standard operating condition, is reduced to 30 Pa.

Another possible disturbance involves the temperature of the gas feeder, which is usually in the form of a bubbler. The temperature variation inside the bubbler can cause a considerable fluctuation of the TDMAHf molar fraction due to the rapid change in the precursor vapor pressure, which is highly dependent on temperature. In this work, a standard operating temperature of 340 K is chosen for the bubbler. In the case study, a disturbance of 10 K drop from the standard operating temperature is explored, which can be commonly seen in the bubbler application (Gaffney et al., 1996). In addition, it is assumed that the inlet stream temperature is still maintained at 340 K through additional heating devices, which is not characterized in this model, so that the bubbler temperature disturbance does not change the thermal environment of the microscopic surface reactions. The open-loop simulation results are shown in Fig. 6, where the impact of the two disturbances can be seen. The coverage of the wafer under the pressure disturbance and the temperature disturbance are 62% and 0.7%, respectively, when the PEALD process is operated without any control action.

3.2. Feedback control formulation and tuning

As mentioned in Section 3, a PI controller is formulated to regulate the process by adjusting the inlet mass flow rate to bring the control variable, i.e., the TDMAHf partial pressure, to the set point. The PI control algorithm is described below:

$$u(t) = K_c(e(t) + \frac{1}{\tau_I}\int_0^t e(t)dt) \tag{13}$$

where t is the process time, K_c and τ_I are the controller gain and time constant, respectively, $u(t)$ is the process input, which is the inlet mass flow rate, and $e(t)$ is the error, which is the deviation between the sensed partial pressure and the set point. The partial pressure set point of 58.3 Pa is chosen for the PI controller according to the steady-state partial pressure of TDMAHf under standard operating condition.

It is also noteworthy that the online monitoring of the precursor partial pressure can be achieved using a pressure sensor and a real-time gas chromatography (GC) device (Sparkman et al., 2011). The pressure sensor is able to measure the total pressure in the reactor via a pressure sensor and generate the corresponding electric signal that is transmitted to the PI controller. Meanwhile, the small amount of gas in the reactor is continuously injected to the GC device to measure the TDMAHf molar fraction. After all, the TDMAHf partial pressure is calculated by multiplying the total pressure by the molar fraction. Then, the PI controller sends the control signal to a flow control valve in accordance with the partial pressure deviation from the set point. The control signal causes the actuator of the valve to move its modulating element and thus, the PI controller is able to adjust the inlet mass flow rate. There are several types of actuators, among which the electric actuator can be used for the PEALD process due to higher level of precision and energy efficiency. The location of the sensor should be carefully selected so that the accurate TDMAHf partial pressure can be obtained since the partial pressure, unlike the total pressure, varies upon the sensor location. The imprecise measurement of the TDMAHf partial pressure can result in invalid control action, which can cause a negative impact on the film quality. In this work, the pressure sensor is installed near the edge of the wafer substrate, along the precursor flow path, to measure the precise TDMAHf partial pressure on the surface as shown in Fig. 7. The control action is executed every 0.2 s due to the sampling limitation of the GC device where the composition analysis is assumed to be implemented every 0.2 s.

In order to ensure the performance of the PI controller, its tuning parameters, K_c and τ_I, must be optimized. First, an approximated process curve is obtained under a step change input through the first order process plus dead-time (FOPDT) approach, which is widely used to identify the relationship between process time and process output (Coughanowr and LeBlanc, 2009). As shown in Fig. 8a, the approximation from the FOPDT model is able to accurately capture the features of the real process behavior. After the process is characterized, the tuning parameters are determined through pre-formulated tuning methods. A variety of tun-

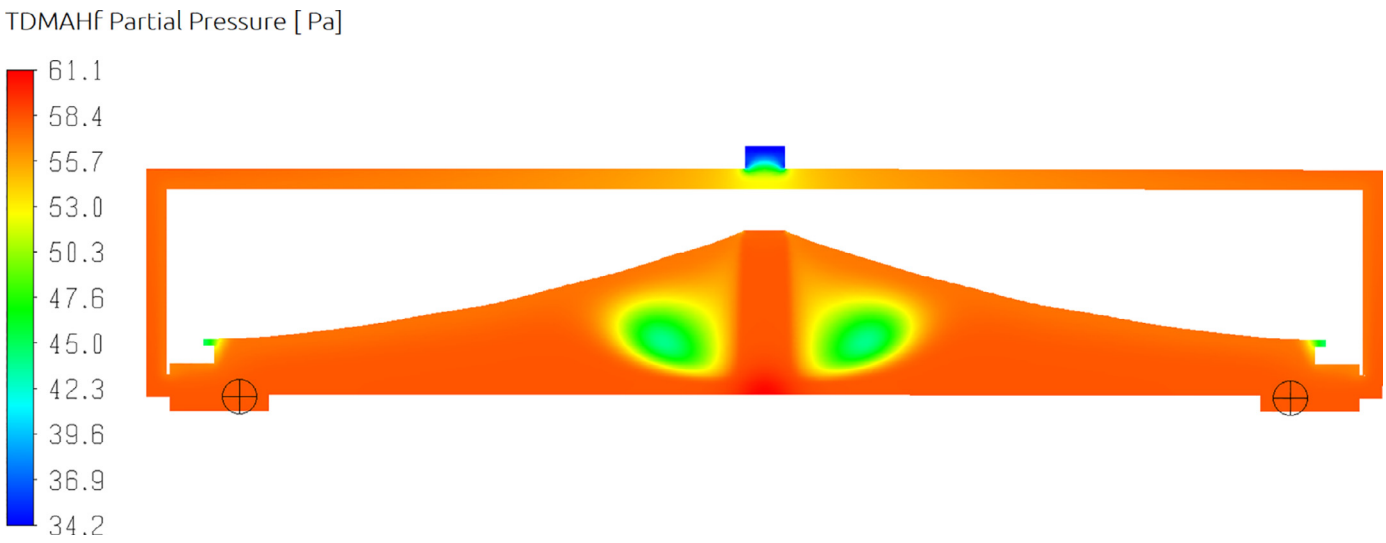

Fig. 7. Multiscale computational fluid dynamics (CFD) model with the TDMAHf partial pressure profile at the end of the batch at the standard conditions. The ⊕ indicates the location of the pressure sensor.

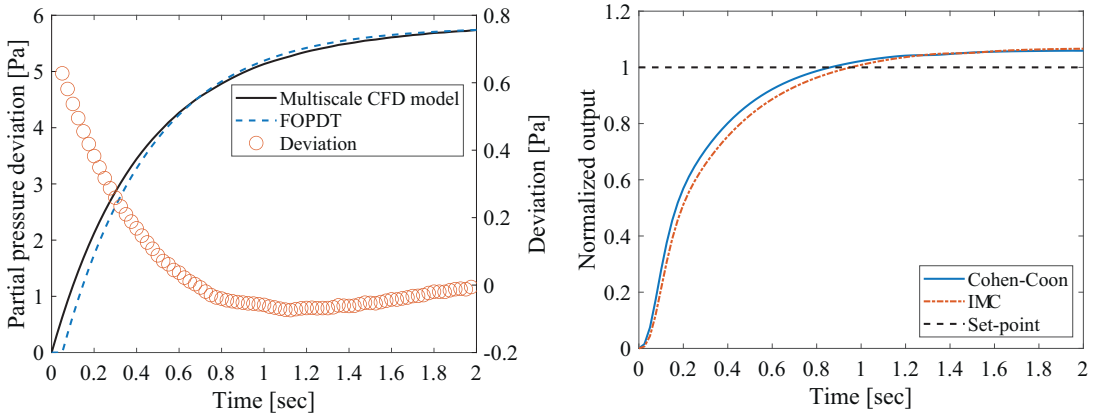

Fig. 8. (a) Error of partial pressure versus the process time. The black solid line denotes the result from the numerical trials using multiscale CFD model. The blue dashed line denotes the process curve fitted using the the FOPDT model approximation and the red circled line shows the deviation from the multiscale CFD model. (b) Normalized partial pressure versus the process time. The black dashed line denotes the set point, which is at 100%, the blue solid line denotes the results using the parameters determined from the Cohen-Coon method, and the red dotted-dashed line denotes the results using the parameters determined from the IMC tuning method. (For interpretation of the references to color in this figure legend, the reader is referred to the web version of this article.)

ing strategies are available and among which the most popular choices are Cohen-Coon (C-C) method and the internal model control (IMC) method. Both methods are tested and the results are demonstrated in Fig. 8b. As indicated by Fig. 8b, the response using the C-C method is 8.6% faster, and the overshoot is approximately 1.0% lower than those from the IMC method. Therefore, in this work, the tuning parameters, K_c and τ_I, are determined using the C-C method, which are obtained to be 2.37×10^{-7} and 0.9113, respectively.

3.2.1. Closed-loop results under feedback controller

The PI controller using the tuning parameters from Section 3.2 is evaluated under the previously stated disturbances where the operating pressure drops to 30 Pa from 100 Pa and the bubbler temperature drops to 338 K from 348 K. According to Fig. 6b, the coverage on the wafer under the pressure disturbance and the temperature disturbance remarkably increases up to 93% from 62% and 47% from 0.7%, respectively. It is demonstrated that the PI controller noticeably diminishes the impact of the disturbances. Nevertheless, the PI control does not completely eliminate the effect of the disturbances. In other words, the PI controller does not guarantee the partial pressure set point of TDMAHf within 2 s, which is the run time determined in Ding et al. (2021). As can be seen in Fig. 6a, the TDMAHf partial pressures under the pressure and temperature disturbances are obtained at the end of the batch as 57.3 Pa and 48.8 Pa, respectively, which are below the set point of 58.3 Pa, thus resulting in an incomplete thin-film deposition. Consequently, the result of the closed-loop PI controller reveals that though the film coverage notably increases, the single control action of the PI controller is not enough to cope with the disturbances. Thus, it is concluded that other control actions must be used to achieve the full coverage on the wafer.

3.3. Run-to-run (R2R) control formulation and parameter determination

Although the PI controller effectively adjusts the inlet flow rate to counter the effect of disturbances on the partial pressure, the limited range of control action fails to provide enough driving force to ensure the quality of the deposited film. As a result, other measures must be taken to improve the film quality by accounting for the differences in partial pressure. Other than manipulating the inlet flow rate, another efficient way to compensate for partial pressure disturbances is to adjust the TDMAHf molar fraction. One op-

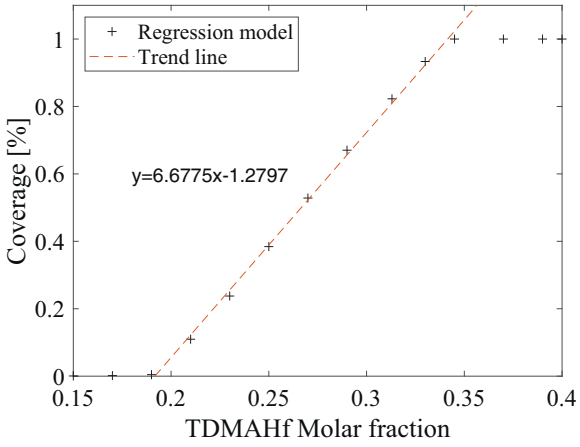

Fig. 9. The input-output relationship between the final film coverage and the precursor molar fraction derived from linear regression used in both EWMA and PCC-based R2R controller. The *y*-axis is the final coverage and the *x*-axis is the inlet TDMAHf molar fraction.

tion is to construct another real-time feedback controller to control the partial pressure by changing the molar fraction. However, the interference between the inlet molar fraction and flow rate in real-time may negatively impact the controller performance. Therefore, a run-to-run (R2R) control methodology, which adjusts the manipulated input after each batch instead of in real-time, is adopted in this study.

A variety of R2R control algorithms have been proposed in the past, among which two are the most popular: the exponentially weighted moving average (EWMA), and the predictor-corrector controller (PCC), which is also known as the double-EWMA (*d*-EWMA). The EWMA algorithm is based on a single-input-single-output (SISO) linear regression model, also known as the input-ouput relationship, which is defined by the following equation:

$$y_t = \alpha + \beta u_{t-1} \tag{14}$$

where y_t is the output of the process at batch number t, α is the offset, β is the process gain, and u_{t-1} is the input (i.e., the manipulated variable) at batch number $t-1$. At the end of every batch, the input is estimated in an iterative manner and expressed as below:

$$u_t = \frac{T - a_t}{\beta} \tag{15}$$

where T is the target value of the output, and the EWMA estimate of the process output a_t is updated by the following equation:

$$a_t = \lambda(y_t - bu_{t-1}) + (1-\lambda)a_{t-1} \tag{16}$$

where λ denotes the weight factor.

On the other hand, the PCC (*d*-EWMA) algorithm is the expanded version of the EWMA. It has two estimates of the process outputs, a_t and d_t, and it uses a modified linear regression model as below:

$$y_t = \alpha + \beta u_{t-1} + \eta_{t-1} \tag{17}$$

where η_{t-1} is the process disturbance and can be assumed to be a white noise. Similar to the EWMA algorithm, the input of PCC algorithm is estimated by the following equation:

$$u_t = \frac{T - a_t - d_t}{\beta} \tag{18}$$

where the estimates of the process output a_t and d_t are updated by the following equations:

$$a_t = \lambda(y_t - bu_{t-1}) + (1-\lambda)a_{t-1} \tag{19}$$

$$d_t = \omega(y_t - bu_{t-1} - a_{t-1}) + (1-\omega)d_{t-1} \tag{20}$$

where λ and ω denote the weight factors.

To formulate the EWMA and the PCC-based R2R controller, the input-output relationship between the inlet TDMAHf molar fraction and the coverage needs to be derived. By running the multi-scale CFD simulation under different inlet TDMAHf molar fractions (the input), the corresponding coverage (the output) is recorded to determine the input-output relationship. As shown in Fig. 9, the linear relationship between the TDMAHf molar fraction and the coverage on the wafer was obtained in the practical operation region in which α and β in Eqs. (14) and (17) are given as -1.2797 and 6.6775, respectively. The range of the operating TDMAHf molar fraction is limited due to the low efficiency and high operating cost. Thus, the upper-limit of the TDMAHf mole fraction is set to be 0.40. The operating TDMAHf mole fraction, 0.345, is chosen so that the full coverage can be achieved within 2 s. After every batch, the parameters a_t and d_t in Eq. (16), (19), and (20) are updated by the weighting factors λ and ω. It is also worth mentioning that, despite the wide acceptance and superior performance of linear input-output relationships, the nonlinear relationship between TDMAHf molar fraction and film coverage can potentially be characterized by a sigmoidal-like nonlinear input-output relationship. However, the asymptotic convergence of the sigmoid function may cause a slow achievement of the desired film quality, or even

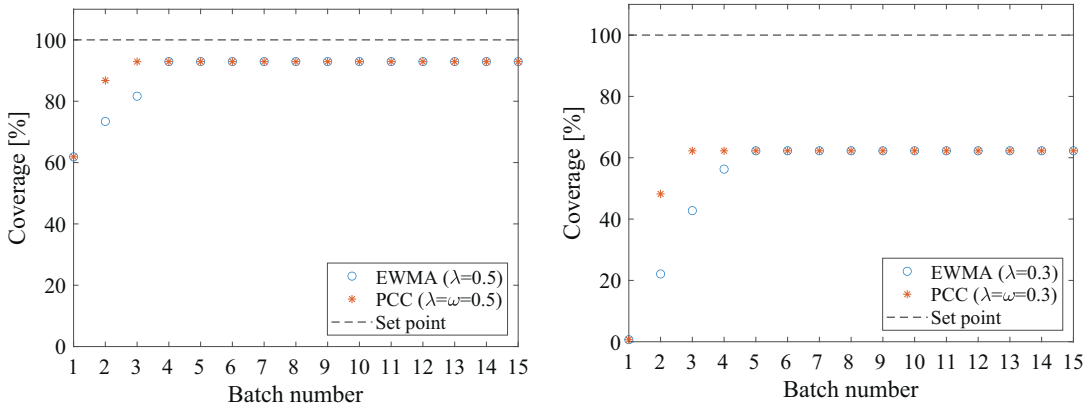

Fig. 10. The final film coverage over fifteen batches under disturbances with only R2R control. The black dashed line represents the film coverage set point, which is at full coverage. The blue dots denote the result using the EWMA algorithm, and the red asterisks denote the result using the PCC algorithm. (a) Under pressure disturbance. (b) Under temperature disturbance. (For interpretation of the references to color in this figure legend, the reader is referred to the web version of this article.)

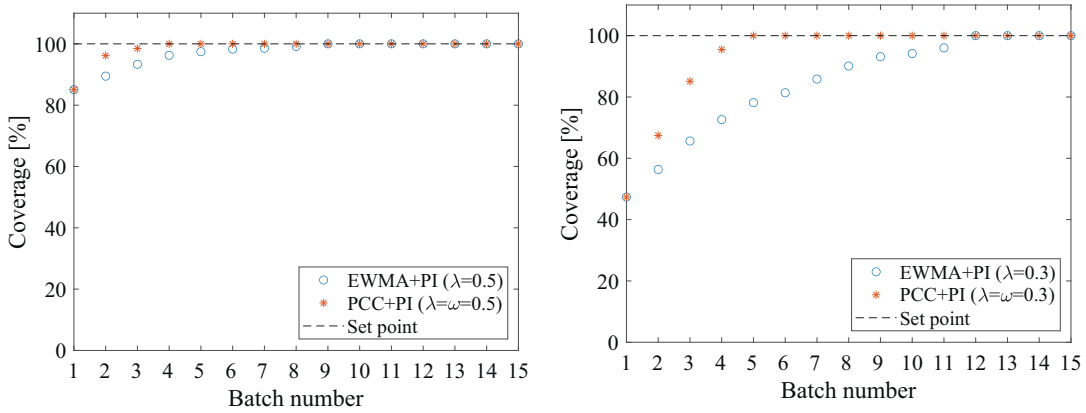

Fig. 11. The final film coverage over fifteen batches under disturbances with the integrated PI-R2R control. The black dashed line represents the film coverage set point, which is at full coverage. The blue dots denote the result using EWMA as the R2R algorithm, and the red asterisks denote the result using PCC as the R2R algorithm. (a) Under pressure disturbance. (b) Under temperature disturbance. (For interpretation of the references to color in this figure legend, the reader is referred to the web version of this article.)

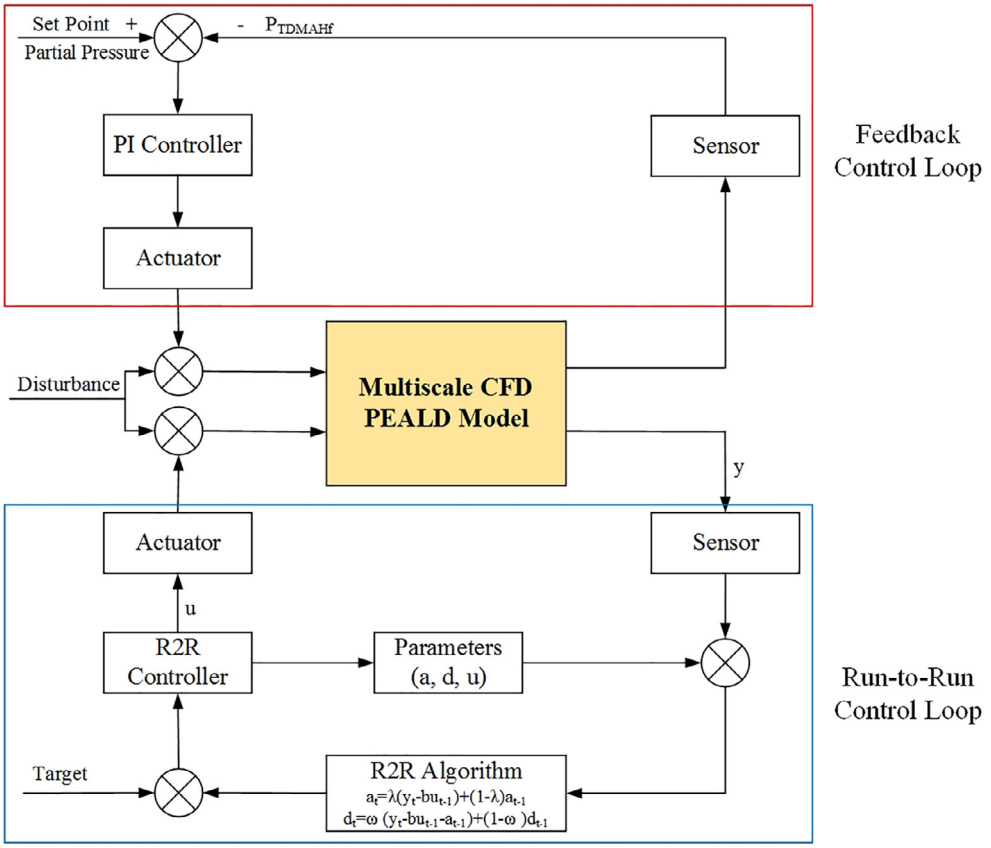

Fig. 12. Operating principle diagram of the feedback controller and the run-to-run (R2R) controller. The red box denotes the feedback control loop, and the blue box denotes the R2R control loop. (For interpretation of the references to color in this figure legend, the reader is referred to the web version of this article.)

cause an offset in the final achievable coverage. Therefore, although there may be benefits adopting a nonlinear input-output relationship, this work will focus on the use of the linear input-output relationship.

3.3.1. Results under run-to-run controller

As indicated in Fig. 10, the PCC-based R2R controller shows faster respond compared to the EWMA-based R2R controller under the disturbances. As shown in the Fig. 10a, the EWMA and PCC-based R2R controller reach the final coverage under the pressure disturbance at batch number 4 and 3, respectively. Likewise, the EWMA and PCC-based R2R controller achieve the final coverage under the temperature disturbance at the batch number 5 and 4, respectively as can be seen in Fig. 10b. Nonetheless, the deposited film coverage is not fully achieved, where a 93 % coverage is reached under the pressure disturbance and a 62 % coverage is reached under the temperature disturbance for the two types of R2R controllers because the updated molar fraction hits the upper limit of the operating rage. The results of the R2R controllers under the disturbances reveals that an additional control action should be taken to ensure the quality of the thin-film.

3.4. Integration of feedback and run-to-run control

As described in the previous sections, even when the parameters of the PI controller and the R2R controller are well tuned,

independently and when used in isolation they are not able to completely reject the effect of the disturbances that can be potentially encountered in the PEALD process. Therefore, the mutual effort of both PI controller and of the R2R controller is required to ensure the robustness of the deposition process against disturbances. Specifically, the controller workflow is shown in the operating principle diagram as in Fig. 12 for both the feedback controller (PI) and the R2R controller (EWMA & d-EWMA). A number of simulation runs using the multiscale CFD model have been carried out to test the performance of the integrated PI-R2R controller. First, the PI controller, formulated in Section 3.2, is used to adjust the inlet mass flow rate during the deposition process. Then, after the first batch has finished, the film coverage is recorded and transferred to the R2R controller. Before the next run, the R2R controller computes the TDMAHf molar fraction of the inlet stream through either the EWMA or the PCC algorithms, of which the performance will be evaluated. The updated TDMAHf molar fraction is then used as the inlet condition for the next run to further eliminate the effect of the disturbances. The same disturbances mentioned in Section 3.1 are used to verify the performance of the integrated PI-R2R controller.

The results of the integrated PI-R2R controller using both EWMA and PCC algorithms in the R2R controller are shown in Fig. 11. As shown in Fig. 11a, the EWMA-based and the PCC-based integrated PI-R2R controllers achieve full coverage on the surface at batch number 9 and 4, respectively, under the same pressure disturbance. Likewise, the EWMA-based and the PCC-based integrated controller reach full coverage at batch number 12 and 5, respectively, under the temperature disturbance as shown in Fig. 11b. Therefore, it is proved that the integrated controller successfully ensures the full coverage of the thin-film under various disturbances. Furthermore, as noted in Section 3.3.1, the PCC-based integrated PI-R2R controller shows faster response than the EWMA-based PI-R2R controller. In particular, the deposition under the regulation of the PCC-based PI-R2R controller achieves full coverage about 60% faster than the EWMA-based integrated PI-R2R controller. Thus, the strategy of integrating the PI controller and R2R controller is validated and can largely improve the process robustness.

4. Conclusion

In this work, the previously developed multiscale CFD model was used to design and evaluate a control strategy that utilizes an integrated PI-R2R controller which adopts both feedback control and R2R control. The designed controller was investigated from both open-loop and closed-loop simulations in the presence of two types of disturbances. To eliminate the effect of the disturbances, first, the PI controller was constructed to ensure the desired TDMAHf partial pressure by adjusting the inlet mass flow rate. Next, the R2R controller was set up to manipulate the inlet TDMAHf molar fraction according to the derived input-output relationship at the beginning of every batch to further ensure the complete deposition and the film conformity. To validate the necessity and the effect of the integrated controller, both the PI and the R2R controller were evaluated independently. These evaluation results demonstrated that individual control actions were not sufficient to guarantee full coverage, and an additional control effort was required. Thus, the R2R controller and the PI controller were integrated to fully eliminate the effect of the disturbances. A corresponding case study using the multiscale CFD model validated that the integrated PI-R2R controller was able to reject the disturbances and achieves the conformity of atomic layer deposition. Furthermore, the results demonstrated that the PCC algorithm used in the R2R controller was able to improve the run-to-run control action and respond approximately 60 % faster than the EWMA algorithm. In the future, research adopting more advanced control method, such as model predictive model using the developed data-driven model, is recommended to optimize the control workflow and maximize control efficiency.

Declaration of Competing Interest

- All authors have participated in (a) conception and design, or analysis and interpretation of the data; (b) drafting the article or revising it critically for important intellectual content; and (c) approval of the final version.
- This manuscript has not been submitted to, nor is under review at, another journal or other publishing venue.
- The authors have no affiliation with any organization with a direct or indirect financial interest in the subject matter discussed in the manuscript
- The following authors have affiliations with organizations with direct or indirect financial interest in the subject matter discussed in the manuscript:

CRediT authorship contribution statement

Sungil Yun: Conceptualization, Methodology, Software, Writing - original draft. **Yangyao Ding:** Conceptualization, Methodology, Software, Writing - original draft. **Yichi Zhang:** Conceptualization, Methodology, Software, Writing - original draft. **Panagiotis D. Christofides:** Writing - review & editing.

Acknowledgments

Financial support from the National Science Foundation is gratefully acknowledged.

References

Armaou, A., Christofides, P.D., 1999. Plasma enhanced chemical vapor deposition: modeling and control. Chem. Eng. Sci. 54, 3305–3314.
Cortright, R.D., Dumesic, J.A., 2001. Kinetics of heterogeneous catalytic reactions: analysis of reaction schemes. Adv. Catal. 46, 161–264.
Coughanowr, D.R., LeBlanc, S.E., 2009. Chapter 18 - controller tuning and process identification. In: Process Systems Analysis and Control. McGraw-Hill Education, pp. 408–418.
Crose, M., Kwon, J.S.-I., Nayhouse, M., Ni, D., Christofides, P.D., 2015. Multiscale modeling and operation of PECVD of thin film solar cells. Chem. Eng. Sci. 136, 50–61.
Crose, M., Zhang, W., Tran, A., Christofides, P.D., 2019. Run-to-run control of PECVD systems: application to a multiscale three-dimensional CFD model of silicon thin film deposition. AIChE J. 65 (7), e16400.
Ding, Y., Zhang, Y., Chung, H.Y., Christofides, P.D., 2021. Machine learning-based modeling and operation of plasma-enhanced atomic layer deposition of hafnium oxide thin films. Comput. Chem. Eng. 144, 107148.
Ding, Y., Zhang, Y., Kim, K., Tran, A., Wu, Z., Christofides, P.D., 2019. Microscopic modeling and optimal operation of thermal atomic layer deposition. Chem. Eng. Res. Des. 145, 159–172.
Ding, Y., Zhang, Y., Orkoulas, G., Christofides, P.D., 2020. Microscopic modeling and optimal operation of plasma enhanced atomic layer deposition. Chem. Eng. Res. Des. 159, 439–454.
Dorsmann, R., Kleijn, C.R., 2007. A general correction to surface reaction models based on reactive sticking coefficients. Chem. Vap. Depos. 13, 91–97.
Epelle, E.I., Gerogiorgis, D.I., 2017. A multiparametric CFD analysis of multiphase annular flows for oil and gas drilling applications. Comput. Chem. Eng. 106, 645–661.
Fluent, A., 2013. ANSYS Fluent Theory Guide 15.0. ANSYS, Canonsburg, PA.
Gaffney, M.S., Reaves, C.M., Smith, R.S., Holmes, A.L., DenBaars, S.P., 1996. Control of IIIV epitaxy in a metalorganic chemical vapor deposition process: impact of source flow control on composition and thickness. J. Cryst. Growth 167 (1), 8–16.
Gakis, G.P., Vahlas, C., Vergnes, H., Dourdain, S., Tison, Y., Martinez, H., Bour, J., Ruch, D., Boudouvis, A.G., Caussat, B., Scheid, E., 2019. Investigation of the initial deposition steps and the interfacial layer of atomic layer deposited (ALD) Al_2O_3 on Si. Appl. Surf. Sci. 492, 245–254.
Gakis, G.P., Vergnes, H., Scheid, E., Vahlas, C., Boudouvis, A.G., Caussat, B., 2019. Detailed investigation of the surface mechanisms and their interplay with transport phenomena in alumina atomic layer deposition from TMA and water. Chem. Eng. Sci. 195, 399–412.
Gerogiorgis, D.I., Ydstie, B., 2005. Multiphysics CFD modelling for design and simulation of a multiphase chemical reactor. Chem. Eng. Res. Des. 83, 603–610.

Hausmann, D.M., Kim, E., Becker, J., Gordon, R.G., 2002. Atomic layer deposition of hafnium and zirconium oxides using metal amide precursors. Chem. Mater. 14, 4350–4358.
Huang, J., Hu, G., Orkoulas, G., Christofides, P.D., 2010. Dependence of film surface roughness and slope on surface migration and lattice size in thin film deposition processes. Chem. Eng. Sci. 65, 6101–6111.
Jeon, H., Won, Y., 2008. The reaction pathways of the oxygen plasma pulse in the hafnium oxide atomic layer deposition process. Appl. Phys. Lett. 93 (12), 124104.
Jeon, H.-T., Kim, I.-H., Kim, S.-H., Chung, C.-W., Lee, S.-K., 2007. Apparatus for Generating Remote Plasma. US Patent App. 11/703,621.
Joo, J., Rossnagel, S.M., 2009. Plasma modeling of a PEALD system for the deposition of TiO_2 and HfO_2. J. Korean Phys. Soc. 54, 1048.
Kanomata, K., Pansila, P., Ahmmad, B., Kubota, S., Hirahara, K., Hirose, F., 2014. Infrared study on room-temperature atomic layer deposition of TiO_2 using tetrakis (dimethylamino) titanium and remote-plasma-excited water vapor. Appl. Surf. Sci. 308, 328–332.
Kukli, K., Ritala, M., Schuisky, M., Leskelä, M., Sajavaara, T., Keinonen, J., Uustare, T., Hårsta, A., 2000. Atomic layer deposition of titanium oxide from TiI_4 and H_2O_2. Chem. Vap. Depos. 6, 303–310.
Kumar, N., George, B.P.A., Abrahamse, H., Parashar, V., Ray, S.S., Ngila, J.C., 2017. A novel approach to low-temperature synthesis of cubic HfO_2 nanostructures and their cytotoxicity. Sci. Rep. 7, 1–14.
Lee, C.S., Oh, M.S., Park, H.S., 2006. Plasma Enhanced Atomic Layer Deposition (PEALD) Equipment and Method of Forming a Conducting Thin Film Using The Same Thereof. US Patent 7,138,336.
Liu, X., Ramanathan, S., Longdergan, A., Srivastava, A., Lee, E., Seidel, T.E., Barton, J.T., Pang, D., Gordon, R.G., 2005. ALD of hafnium oxide thin films from tetrakis (ethylmethylamino) hafnium and ozone. J. Electrochem. Soc. 152, G213–G219.
Liu, X., Ramanathan, S., Seidel, T.E., 2003. Atomic layer deposition of hafnium oxide thin films from tetrakis (dimethylamino) hafnium (TDMAH) and ozone. MRS Online Proc. Lib. Arch. 765.
Profijt, H., Potts, S., Van de Sanden, M., Kessels, W., 2011. Plasma-assisted atomic layer deposition: basics, opportunities, and challenges. J. Vac. Sci. Technol. A 29, 050801.
Rai, V.R., Vandalon, V., Agarwal, S., 2010. Surface reaction mechanisms during ozone and oxygen plasma assisted atomic layer deposition of aluminum oxide. Langmuir 26, 13732–13735.
Shi, X., Tielens, H., Takeoka, S., Nakabayashi, T., Nyns, L., Adelmann, C., Delabie, A., Schram, T., Ragnarsson, L., Schaekers, M., et al., 2011. Development of ALD $HfZrO_x$ with TDEAH/TDEAZ and H_2O. J. Electrochem. Soc. 158, H69–H74.
Shirazi, M., Elliott, S.D., 2014. Atomistic kinetic Monte Carlo study of atomic layer deposition derived from density functional theory. J. Comput. Chem. 35, 244–259.
Sparkman, D.O., Penton, Z.E., Kitson, F.G., 2011. Chapter 2 - gas chromatography. In: Gas Chromatography and Mass Spectrometry, pp. 15–83.
Tinck, S., Bogaerts, A., 2011. Computer simulations of an oxygen inductively coupled plasma used for plasma-assisted atomic layer deposition. Plasma Sour. Sci. Technol. 20, 015008.
Won, T.K., Nominanda, H., Cho, S.-M., Choi, S.Y., Park, B.S., White, J.M., Anwar, S., Kudela, J., 2014. Thin Film Deposition Using Microwave Plasma. US Patent 8,883,269.
Won, Y., Park, S., Koo, J., Kim, S., Kim, J., Jeon, H., 2005. Initial reaction of hafnium oxide deposited by remote plasma atomic layer deposition method. Appl. Phys. Lett. 87, 262901.
Yun, S.J., Lim, J.W., Lee, J.-H., 2004. PEALD of zirconium oxide using tetrakis (ethylmethylamino) zirconium and oxygen. Electrochem. Solid-State Lett. 7, F81–F84.
Zhang, Y., Ding, Y., Christofides, P.D., 2019. Multiscale computational fluid dynamics modeling of thermal atomic layer deposition with application to chamber design. Chem. Eng. Res. Des. 147, 529–544.
Zhang, Y., Ding, Y., Christofides, P.D., 2020. Integrating feedback control and run–to-run control in multi-wafer thermal atomic layer deposition of thin films. Processes 8, 18.
Zhang, Y., Ding, Y., Christofides, P.D., 2020. Multiscale computational fluid dynamics modeling and reactor design of plasma-enhanced atomic layer deposition. Comput. Chem. Eng. 147, 107066.